The Adsorption Performance of MoS$_2$ Nano-rod by Combined with Graphene Oxide for Cr(VI) Removal from Aqueous Solution

Jing ZHOU [1], **Chongdian SI** [2]*, **Hongtao GAO** [3]

[1] *Department of Energy and Material Engineering, Shandong Polytechnic College, Jining 272400, China*

[2] *Shandong Engineering Research Center of Chemical Intermediate, Jining University, Qufu 273155, China*

[3] *College of Chemistry and Molecular Engineering, Qingdao University of Science & Technology, Qingdao, 266042, P. R. China*

The rod-like nano-MoS$_2$/graphene oxide (GO) nanocomposite was fabricated by a facile hydrothermal method, which was characterized by X-ray diffraction (XRD), scanning electron microscope (SEM) and N$_2$ adsorption–desorption isotherms, respectively. It was used as adsorbent to remove heavy metal contaminate, such as Cr(VI), from aqueous solution. The investigations on adsorption kinetics and isotherms showed that the pseudo-second-order kinetic and Langmuir isotherm model could well fit the experimental data. The adsorption rate was controlled by both exterior and interior surface diffusion steps. Further investigations on the activation energy and thermodynamics of the adsorption process elucidated that the Cr(VI) adsorption on MoS$_2$/GO was an endothermic and spontaneous chemi-sorption process. The maximum adsorption capacity was 43.95 mg·g^{-1} and the adsorption efficiency of Cr(VI) was enhanced significantly with the coexistence of organic contamination. After recycling five times, the decline of adsorption capacity of MoS$_2$/GO was no more than 8.0 %, which indicated that the adsorbents could be reused in Cr(VI) removal practically. The MoS$_2$/GO nanocomposite has been proved to be a low-cost, efficient and promising adsorbent used for heavy metal ions removal from wastewater.

Keywords: MoS$_2$/GO nanocomposite, Cr(VI) removal, adsorption capacity, adsorption mechanism.

1. INTRODUCTION

The environmental pollutions have been eliciting numerous concerns, which are closely related to daily lives as well as directly determined the safety of human survive. The heavy metal contaminant, such as chromium, has brought a serious threat to the ecological environment and to human survival. It has become an urgent problem to solve heavy metal contaminant [1]. The stable oxidation states of chromium exist in nature include Cr(III) and Cr(VI). And Cr(VI) is highly toxic and carcinogenic to living organisms. According to the report from World Health Organization(WHO), the maximum allowable content for Cr(VI) discharges into inland surface waters was at the level of 0.1 mg·L^{-1} [2]. Therefore it has been most important to remove Cr(VI) from the contaminated water environment. At present, some physical and chemical methods, such as adsorption, ion exchange, dialysis, precipitation and extraction, have been used to remove Cr(VI) from wastewater [3]. Among these methods, adsorption is one of the most economically favorable and effective technology. And the properties of adsorbent influenced on the adsorption removal efficiency significantly [4]. Therefore, it is an urgent task to find adsorbents with excellent properties to improve the adsorption efficiency for heavy metal contaminant from wastewater. Molybdenum disulfide (MoS$_2$) is a representative transition metal dichalcogenide with a layered structure composed of three stacked atom layers (S-Mo-S) similar sandwich, which holds strong covalent bonding between Mo-S atomic but weak van der Waals attraction between lattice layers [5]. Up to date, nano-MoS$_2$ has attracted tremendous attention owing to its unique triangular prismatic structure, large surface area, high surface activity and electron-transport property. The investigation on nano-MoS$_2$ has found that Mo edge-site atoms became chemically active without the protection from the inert basal planes of MoS$_2$ when its size decreased to nanoscale [6]. MoS$_2$ with different morphologies have been reported for electrochemical and electrode material, catalysis, such as nanoplates, nanoflakes, nanotubes and nanoflower [7]. However, its potential application in the important area of environmental cleanup has not yet been effectively explored. And there are few reports on its adsorption properties of MoS$_2$. Nanostructured MoS$_2$ has been used as a regenerative adsorbent for efficient removal of dyes from wastewater [8]. MoS$_2$ nanosheets with widened interlayer spacing exhibited high efficiency removal of mercury in aquatic systems [9].The inherent stacking nature among MoS$_2$ layers seriously limits the amount of exposed active sites. In order to improve its activity, it is of great importance to increase the exposed active sites and prevent the stacking and aggregation of MoS$_2$ layers [10]. Reduced graphene oxide (RGO) could preventrestacking of MoS$_2$ layer, resulting in mesoporous structure,

whichenhanced adsorption effect [11]. After polyaniline-modified 3D flower-like MoS_2 can be applied in efficient adsorption removing Cr(VI) ions from an aqueous solution [12].

Owing to its outstanding electronic behavior, large surface area and superior chemical stability, graphene, the thinnest two-dimensional carbon nanomaterial, has attracted more and more attention in recent years [13]. After oxidized to graphene oxide (GO), not only the interlayer spacing became larger but also the functional groups on the surface of GO increased, which brought much more active sites. Few-layered graphene oxide nanosheets were used as superior sorbents for the removal of Cd(II) and Co(II) ions from aqueous solutions [14]. It has been reported that Pb(II) ion adsorption performance of few-layered graphene oxide was increased greatly by abundant oxygen-containing groups on its surface [15]. It has revealed that GO played a significant role in promoting the adsorption efficiency of heavy metal ions and degradation of organic dyes for the graphene-based adsorbents [16, 17]. Therefore, as a novel adsorbent, MoS_2/GO composites consisting of nano-MoS_2 layer with a 2D layer might have great significance and potential applications in removal of heavy metal ions from wastewater. However, to the best of our knowledge, there were few reports on the application of MoS_2/GO nanocomposite as a high efficient adsorbent for heavy metal removal.

In this work, rod-like nano-MoS_2/GO has been fabricated by a facile hydrothermal synthesis. The product was characterized by X-ray diffraction (XRD), scanning electron microscopy (SEM) and N_2 adsorption-desorption isotherm (BET). Batch experiments were carried out to investigate the adsorption performance of nano-MoS_2/GO nanocomposites. The investigation on the adsorption kinetics, thermodynamics and isotherm were carried out to study the possible mechanism of Cr(VI) adsorption on the surface of nano-MoS_2/GO adsorbent. Furthermore, the sorption/desorption and reusability of the adsorbent was explored to its sustainability.

2. EXPERIMENTAL

2.1. Materials

All chemicals and reagents used in the experiments were analytical grade and used without further purification. Ultrapure water was used in the whole experiments. Sodium molybdate dehydrate ($Na_2MoO_4 \cdot 2H_2O$) and graphite powder were purchased from Sinopharm Chemical Reagent Co., Ltd. (Shanghai, China). Thioacetamide (CH_3CSNH_2) was commercially available from Tianjin Guangfu Fine Chemical Research Institute. Citric acid ($C_6H_8O_7 \cdot H_2O$) was supplied by Yantai Sanhe Chemical Reagent Co., Ltd. The graphene used in this work was synthesized by modified Hummer method [18].

2.2. Synthesis of absorbents

In this work, MoS_2/GO nanocomposite was synthesized via a simple one-step hydrothermal method. In a typical synthesis, a certain amount of graphite powder (ca. 20 mg) were dissolved in 30 mL ultrapure water to form dark gray suspension, which was then put under ultrasonic treatment for 1 h. Certain amounts of $Na_2MoO_4 \cdot 2H_2O$ (0.50 g) and CH_3CSNH_2 (ca. 0.80 g) were used as Mo and S sources, and added into above suspension, respectively. The suspension was stirred magnetically for about 30 min at speed of 1000 rpm until forming a homogeneous brown solution. A certain amount of citric acid (ca. 0.21 g) was added to the foregoing mixed solution with continuing stir to enhance its dispersion. After being magnetically stirred for 20 min, the obtained suspension was transferred to a 50 ml Teflon-lined stainless steel autoclave and maintained at 220 °C for 24 h. After cooling to the ambient temperature naturally, a black curd-like precipitate was collected and washed with ultrapure water three times firstly, and then washed with absolute alcohol three times, finally dried in an oven at 333 K overnight to obtain the product. The experimental process was represented in the schematic diagram below.

2.3. Characterization

A scanning electron microscope JSM-6300 (JEOL Ltd, Japan) was used to investigate the surface morphology of the sample under the specified conditions of 20 keV, 16 mm working distance, and 5000 magnification. In addition, the quantitative element identification was carried out by Energy Dispersive Spectroscopy (EDS). The crystalline phase of the powders was examined by X-ray diffraction (XRD), which was carried out on a Bruker D8 advance X-ray diffractometer equipped with graphite monochromatized Cu Kα radiation ($\lambda = 1.54056$ Å) operated at 45 kV and 40 mA. The N_2-based Brunauer-Emmett-Teller (BET) surface area of products was determined at 77 K by the surface area analyzer (ASAP 2020 V4.01) with low pressure dose 10.000 cm^3/g STP and equilibration interval 30 s. Infrared (IR) spectroscopy was recorded on a Fourier transform infrared spectroscopy (FTIR) spectrometer (Nicolet IS10) and only major peaks are reported in inverse centimeters. Malvern Zetasizer Nano (ZS90) was used to determinate the particle size and dispersion of the adsorbent. And the concentration of the residual Cr(VI) in the adsorption process was measured using an atomic absorption spectrophotometer (TAS-987, Beijing Purkinje General Instrument Co., Ltd., China).

2.4. Adsorption experiments

The adsorptive performance of MoS_2/GO for Cr(VI) removal from aqueous solution was evaluated. The adsorption experimental procedure is shown in Fig. 1. The product was filled and fixed in a glass column. The Cr(VI) solution was introduced into the column through the peristaltic pump from the bottom the column. Cr(VI) was adsorbed on the adsorbent after the solution flew through column. At predetermined time intervals, 1.5 mL of aqueous suspension was taken from the flask, centrifuged and filtered through a 0.45 μm millipore filter to determine the concentration of Cr(VI). And the concentration of the residual Cr(VI)

in the adsorption process was measured using a UV-vis spectrophotometer with the wavelength at 540 nm by diphenylcarbazine method.
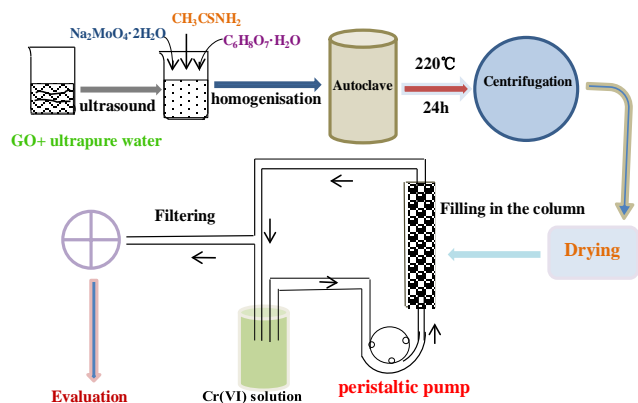

Fig. 1. Experimental procedure

The removal efficiency (*R*) and the amount of Cr(VI) adsorbed on the MoS$_2$/GO at equilibrium are calculated from the Eq. 1 and Eq. 2:

$$R\% = \frac{C_0 - C_t}{C_0} \times 100\% \; ; \tag{1}$$

$$q_e = \frac{(C_0 - C_e)V}{m} . \tag{2}$$

The amount of adsorbed Cr(VI) at any time *t* was calculated according to the Eq. 3:

$$q_t = \frac{(C_0 - C_t)V}{m} , \tag{3}$$

where C_0 represents the concentration of Cr(VI) (mg·L^{-1}) at initial time, C_t is the concentration at any time (*t*) and C_e denotes the concentration at equilibrium, respectively; q_e (mg·g^{-1}) and q_t (mg·g^{-1}) mean the equilibrium absorption capacity and the adsorption capacity of adsorbent at time *t*, individually; *V*(L) and *m* (g) are the volume of the solutions and the mass of adsorbent.

3. RESULTS AND DISCUSSION

3.1. XRD analysis

The measured XRD patterns of MoS$_2$ and MoS$_2$/GO are displayed in Fig. 2. There was one characteristic diffraction peak (14.38°) in XRD of MoS$_2$, which corresponded to the (002) plane of hexagonal MoS$_2$ (JCPDS#73-1508). And the weak peaks of 32.80° and 58.56° could be indexed to the (100) and (110) planes of MoS$_2$. The typical diffraction peaks of MoS$_2$/GO at 2θ = 14.38°, 32.80°, 33.6°, 39.65° and 58.56° correspond to (002), (100), (101), (103) and (110) planes of the standard card of MoS$_2$, respectively. Compared to that of MoS$_2$, there appeared a peak near the significant characteristic peak lied at 14.38°, which indicated the layer spacing of MoS$_2$ was enlarged by the combining of GO. The significant characteristic peak lied at 14.38° changed hardly, which meant GO combination had not affected the crystallinity of MoS$_2$/GO. There appeared a characteristic peak, located at

13.3°, which indexed to GO (001). The measure of the diffraction peak might be error caused by instrument condition. The deviation of the diffraction peak might be caused by the working conditions of instrument.
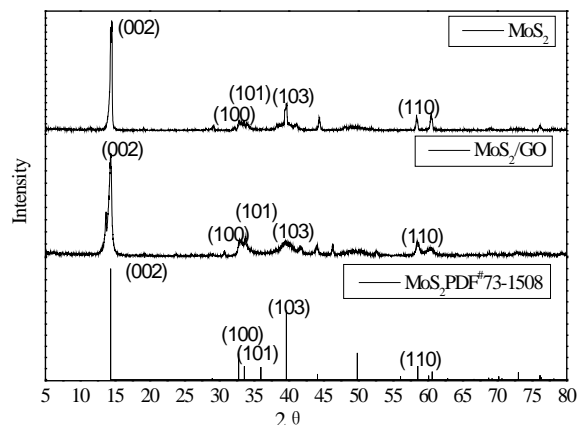

Fig. 2. XRD patterns for the MoS$_2$ and MoS$_2$/GO composites

3.2. SEM analysis

The scanning electron microscope (SEM) was adopted to investigate the surface morphology and particles distribution of the product. As shown in Fig.3a, MoS$_2$/GO showed stacked structure contained by some local networks, which linked nanorods together. The local networks were thin layers, which might be considered as GO sheets. In order to confirm the chemical composition of the as-prepared structures, energy dispersive spectrometer (EDS) was taken at a number of selected positions of the sample. The elemental signatures of Mo, S, C and O were observed from Fig. 3 b, which elucidated that GO was hybridized into the composite. The atomic ratio of Mo, S, C and O on a typical selected surface was 0.84:2.69:67.82:28.65.
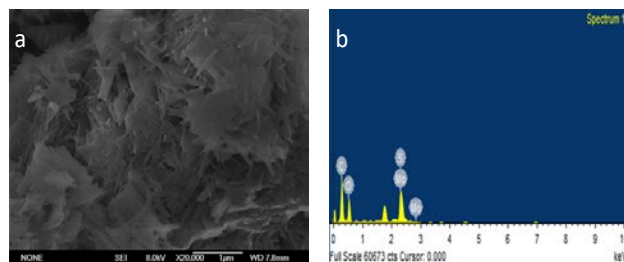

Fig. 3. a – SEM; b – EDS of MoS$_2$/GO composites

3.3. IR analysis

The FTIR spectrum of MoS$_2$/GO is shown in Fig. 4. Obviously, all the characteristic peaks appeared in the spectra reflect the possible existence of functional groups. The broad strong absorption peak at 3436 cm^{-1} corresponded to O–H vibration. The peak appeared at 1630 cm^{-1} was indexed to the bending vibration absorption peak of C–OH. The peak at 1400 cm^{-1} was derived from the C–C stretching vibration of the graphene skeleton. The adsorption peak at 1114 cm^{-1} was the vibration of C–O–C. It indicated there were at least three functional groups, such as –OH, –COOH and C–O–C, existed in graphene oxide sample. The weak peak of 1217, 1140 and 1064 cm^{-1} might

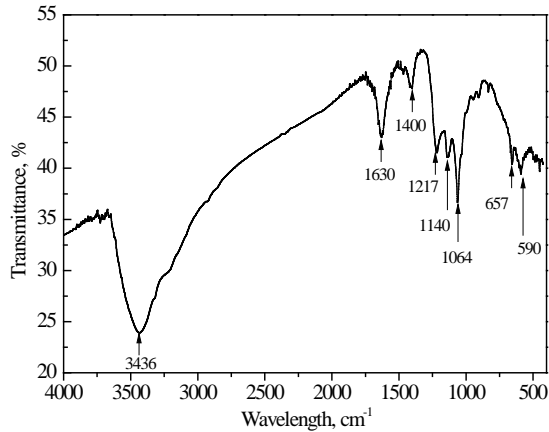belong to C-O vibration. The fingerprints from 590 or 657 cm^{-1} might character the vibration of Mo–O bond.

Fig. 4. The FTIR spectrum of MoS$_2$/GO

3.4. N$_2$ adsorption–desorption analysis

The specific surface area and pore size of the prepared MoS$_2$/GO were measured by the Brunauer-Emmet-Teller (BET) method. The N$_2$ adsorption-desorption isotherm curves of MoS$_2$ and MoS$_2$/GO are presented in Fig. 5, which showed that the hysteresis loop appeared in the adsorption/desorption process. With regard to the MoS$_2$, the typical hysteresis loop and sharp increase in N$_2$ adsorption at the larger P/P0 (> 0.5) arise from condensation of N$_2$ in the larger pores. The pore size distributions were determined using the BJH conventional method. The calculated specific surface area of MoS$_2$/GO based on BET data was 4.58 m^2/g with an average pore size of 11.28 nm. While for MoS$_2$, the data were 1.54 m^2/g and 11.12 nm respectively. The specific surface area of MoS$_2$/GO was three times higher than that of pure MoS$_2$, which was attributed to the hybridization of GO. It might exhibit excellent adsorptive performance for the adsorption removal of heavy metal ions.
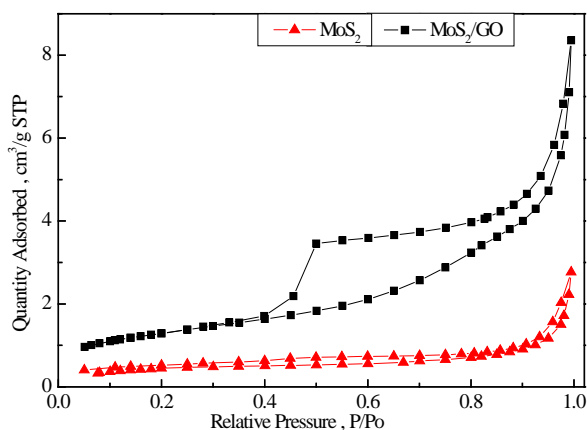

Fig. 5. N$_2$ adsorption-desorption isotherm curve of MoS$_2$ and MoS$_2$/GO nanocomposites

3.5. Adsorption capacities

Adsorption experiments were carried out by adding 0.20 g of MoS$_2$/GO adsorbent to 100 mL Cr(VI) solution at ambient temperature (25 °C). The effect of contact time on the adsorption capacity of GO, MoS$_2$ and MoS$_2$/GO for Cr(VI) at various initial concentrations (25, 50, 75, 100, 125 mg/L) in aqueous solution were presented in Fig. 6. As depicted in the Fig. 6, the adsorption capacities increased quickly at the initial period of the adsorptive process, then increased slowly to reach the plateau. It indicated that the adsorption performance of MoS$_2$/GO was much more than those of both GO and MoS$_2$.
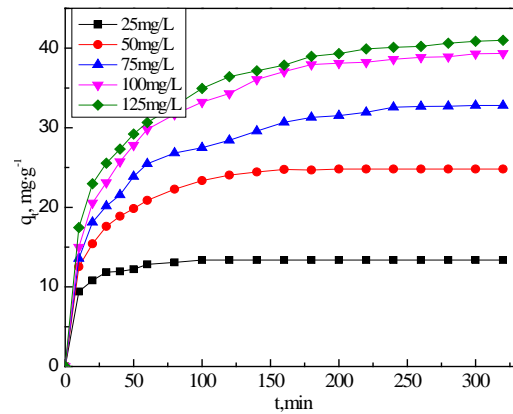

Fig. 6. The adsorption capacities of GO, MoS$_2$ and MoS$_2$/GO for Cr(VI) with various initial concentrations

Due to the properties of pore structure and specific surface area, there were abundant available active sites on the surface of MoS$_2$/GO, which led to the fact that Cr(VI) was rapidly absorbed on MoS$_2$/GO at the initial stage of adsorption. After a period of reaction, since the adsorption sites gradually reached saturation, the adsorption rate decreases before reaching the adsorption equilibrium [19]. The adsorptive rate varied with different initial concentrations. The smaller initial concentration was, the shorter time to reach the equilibrium, which was attributed to the effect of concentration. It reached equilibrium in no more than 100 min when the initial concentration was 25 mg·L^{-1}, while it exhausted about 200 min to reach equilibrium when the concentration increased to 125 mg·L^{-1}. The experimental result showed that the adsorption capacity at equilibrium (q_e) increased from 13.37 to 40.96 mg·g^{-1} when the initial concentration enhanced from 25 mg·L^{-1} to 125 mg·L^{-1}.
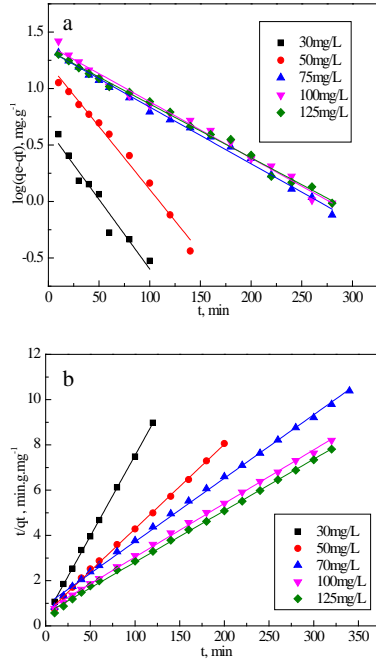
3.6. Adsorption kinetics

The pseudo-first-order and pseudo-second-order kinetic models and the intra-particle diffusion kinetic model were investigated to understand the adsorptive behaviour of Cr(VI) adsorption on the surface of MoS$_2$/GO [20]. The pseudo-first-order kinetic model is expressed in linear form as the following equation:

$$\log(q_e - q_t) = \log q_e - \frac{k_1}{2.303}t \cdot \qquad (4)$$

The pseudo-second-order kinetic model is presented in Eq. 5:

$$\frac{t}{q_t} = \frac{1}{k_2 q_e^2} + \frac{t}{q_e}, \qquad (5)$$

where q_e (mg·g^{-1}) and q_t (mg·g^{-1}) are the adsorption capacities at equilibrium and at any time t, k_1 (min^{-1}) and k_2 (g·mg^{-1}·min^{-1}) is the rate constant for pseudo-first-order and pseudo-second-order respectively. The values of k_1 and k_2 can be determined from the slope of the linear plot of $log(q_e-q_t)$ versus t (Fig. 7 a) and t/q_t versus t (Fig. 7 b), respectively.

Fig. 7. a−pseudo-first-order kinetics; b−pseudo-second-order kinetics for adsorption of Cr(VI) on MoS₂/GO

The kinetics constants of Cr(VI) adsorption on MoS₂/GO are summarized in Table 1. It indicated that the kinetic rate constants (k_1, k_2) decreased with initial concentration increased. The larger initial concentration of Cr(VI) was, the more time to reach adsorption equilibrium spent.

Here, $q_{e,cal}$ and $q_{e,exp}$ indicated the theoretical value of adsorption capacity at the equilibrium and the corresponding experimental value individually. It implied that pseudo-first-order model could not describe the whole adsorption process accurately from Fig. 7. The correlation coefficients (R^2) of pseudo-second-order kinetic model of various concentrations were all higher than those of the pseudo-first-order kinetic model, as presented in Table 1. And significantly, the calculated values ($q_{e,cal}$) were very closer to experimental values ($q_{e,exp}$), confirming the applicability of pseudo-second-order model to describe the whole adsorption process on Cr(VI) on the

MoS₂/GO. Since the Cr(VI) adsorption on MoS₂/GO fit with the pseudo-second-order kinetic model, the adsorption process appeared to be controlled by chemisorption involving valence force through sharing or exchanging of electrons between adsorbate and adsorbent.

To further understand the adsorption process and the possible mechanism of Cr(VI) adsorption onto MoS₂/GO, the intra-particle diffusion model was applied to analyse and simulate the experimental data. The intra-particle diffusion kinetic model was an empirical functional formula based on the theory or equation confirmed by Weber and Morris, which was applied to most adsorption processes. The rate parameter for intra-particle diffusion was determined by the following equation:

$$q_t = K_{di}t^{1/2} + C_i, \qquad (6)$$

where k_{di} is the intra-particle diffusion rate constant (g·mg^{-1}·min$^{1/2}$), the thickness of the boundary layer can be explained based on the values of C_i, the larger the intercept is, the greater the boundary layer effect is. The adsorbate uptaking varies almost proportionally with $t^{1/2}$ rather than with the contact time t. k_{di} and C_i can be calculated from the intercept and slope of the straight-line plot of q_t versus $t^{1/2}$ (Fig. 8), respectively.
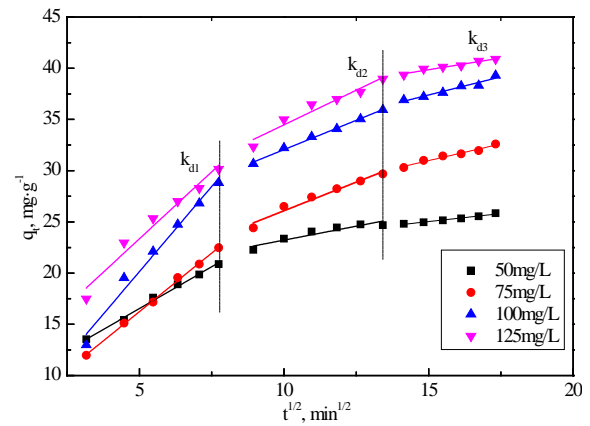
Fig. 8. The intra-particle diffusion kinetics of MoS₂/GO

If the regression of q_t ver $t^{1/2}$ is linear and passthrough the origin zero point, then intra-particle diffusion is regarded as only the rate-controlling step.

If the plot shows multi-linearity, this suggests that adsorption involves intra-particle diffusion, but also be governed by film diffusion [21]. As shown in the Fig. 8, the curves generally exhibited three-linearity, implying there were three steps in the adsorption process.

Table 1. Pseudo-first-order and pseudo-second-order kinetic constants of Cr(VI) adsorption on MoS₂/GO

| C_0, mg·L^{-1}	$q_{e,exp}$, mg·g^{-1}	Pseudo-first-order			Pseudo-second-order		
		$q_{e,cal}$, mg·g^{-1}	k_1, min^{-1}	R^2	$q_{e,cal}$, mg·g^{-1}	k_2, min^{-1})	R^2
25	13.37	4.30	0.0283	0.9432	14.03	0.0126	0.9997
50	24.82	16.58	0.0256	0.9862	26.78	0.00251	0.9989
75	32.72	21.79	0.0116	0.9954	35.65	0.00086	0.9984
100	39.29	24.06	0.0114	0.9902	42.19	0.00084	0.9989
125	40.96	26.84	0.0109	0.9828	43.92	0.00065	0.9989

24

Table 2. Intra-particle diffusion kinetics constants of Cr(VI) adsorption on MoS$_2$/GO nanomaterials

Sample	k_1, g·mg^{-1}·min^{-1}	k_2, g·mg^{-1}·min^{-1}	k_3, g·mg^{-1}·min^{-1}	R_1^2	R_2^2	R_3^2
50	1.633	0.6624	0.00345	0.9932	0.8697	0.9759
75	2.688	1.185	0.6525	0.9979	0.9617	0.9654
100	2.454	1.145	0.7088	0.9778	0.9939	0.9368
125	2.6157	1.352	0.4579	0.9629	0.9553	0.9556

The slopes of three stages were listed in Table 2 and the values of k_{di} determined the adsorption speed. k_{d1}, k_{d2}, k_{d3} were the rate parameters of the exterior surface diffusion, interior pore diffusion and the final equilibrium stage, respectively. Since these straight lines did not pass through the original zero point, the intra-particle diffusion of Cr(VI) adsorption on MoS$_2$/GO was not the only rate-controlling step. The first section of the linear with the fastest adsorption speed might be in the result of the film diffusion, in which Cr(VI) transported from the bulk solution to the external surface of MoS$_2$/GO. Those active sites distributed on the external surface were sufficient to combine and integrate Cr(VI) on MoS$_2$/GO. The second linear region represented the pore diffusion, the active sites on the surface of MoS$_2$/GO were successively occupied and Cr(VI) diffused from surface into pore of MoS$_2$/GO, which was gradually slow and assumed to be the rate-determining step in intra-particle diffusion. The last linear portion described the adsorption equilibrium stage, in which the adsorption sites in both surface and pores of MoS$_2$/GO have been almost completely occupied. In this stage, the adsorption speed hardly changed and became a constant value. That was to say, the adsorption reached saturation gradually. The k_{di} values followed the order of $K_{di1} > K_{di2} > K_{di3}$, which indicated that the amount of Cr(VI) in solution reduced with the adsorption speed slowed down gradually until adsorption equilibrium reached. This might be caused by strong concentration effect of Cr(VI) in its adsorption on MoS$_2$/GO, which conformed the effect of concentration elucidated in the above section.
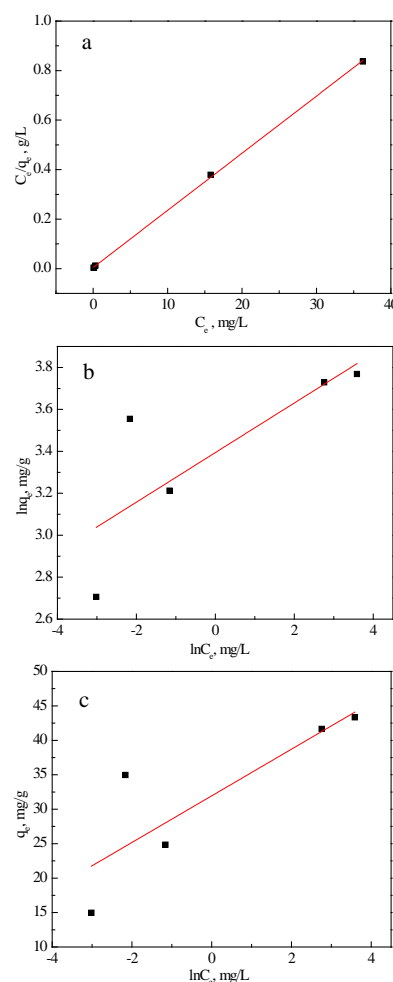
3.7. Adsorption isotherms

Since it gives information about the interactions between adsorbate and adsorbent, fitting experimental data to appropriate isotherm model is necessary in this investigation. The experimental data with initial concentrations varied from 25 to 125 mg·L^{-1} were fitted with three basic adsorption isotherm models (Langmuir, Freundlich and Temkin) tocalculate the maximum adsorption capacity.

3.7.1. Langmuir isotherm

Langmuir isotherm model assumes that a monomolecular layer sorption on homogeneous surface of the adsorbent. And the binding strength of adsorption on a solid surface is same as the binding site, no interaction between the sorbent molecules is found. What's more, each adsorption sites can only accommodate an adsorbate molecule,and an adsorption sitedoesn't produce adsorption again when adsorbate molecule occupies the site [22]. The Langmuir isotherm can be represented as follows:

$$\frac{C_e}{q_e} = \frac{C_e}{q_{max}} + \frac{1}{K_L q_{max}}, \qquad (7)$$

where C_e is the concentration of Cr(VI) (mg·L^{-1}) at equilibrium, q_e and q_{max} (mg·g^{-1}) are the absorption capacity at equilibrium and the maximum adsorption capacity for monolayer formation on adsorbent, respectively; k_L (L·mg^{-1}) is the Langmuir constant related to the maximum adsorption capacity and the energy of adsorption. The values of q_{max} and k_L can be estimated via the slope and intercept of the linear plot of C_e/q_e versus C_e, as shown in Fig. 9 a.

Fig. 9. a – Langmuir; b – Freundlich; c – Temkin adsorption isotherm for Cr(VI) on MoS$_2$/GO

3.7.2. Freundlich isotherm

Freundlich isotherm model is an empirical model which assumes that sorption takes place on a heterogeneous surface and active sites with varied energies, not restricted to monolayer sorption alone but

also be applied multilayer adsorption. The linear form of the Freundlich isotherm model is described as Eq. 8:

$$\ln q_e = \ln K_F + \frac{1}{n}\ln C_e,\qquad(8)$$

where K_F (mg·g^{-1}(L·mg^{-1})$^{1/n}$) and n are Freundlich constants affecting the adsorption capacity and adsorption intensity respectively. By the plot of lnq_e against lnC_e, the values of K_F and $1/n$ could be obtained from the intercept and slope of the liner, as shown in Fig. 9 b, respectively. The value of $1/n$ ranges between 0 and 1 and was an empirical parameter related to the adsorption intensity or surface heterogeneity [23], $n > 1$ represent easier adsorption and favourable adsorption condition.

3.7.3. Temkin isotherm

Temkin isotherm model is the model taking into account the effects of indirect adsorption interaction and adsorption substances on adsorption isotherms depended on the assumptions as following: first of all, the adsorptive heat ofall the molecules in the layer decreases linearly with increasing surface coverage as result of adsorbent/adsorbate interactions rather than logarithmic as implied in Freundlich isotherm [24], secondly, bounding energies are distributed uniformly up to some maximum bonding energy. The Temkin model is expressed in linear form using the following equation:

$$q_e = B\ln K_t + B\ln C_e,\qquad(9)$$

where, K_t (L·g^{-1}) is the equilibrium binding constant corresponding to the maximum binding energy and B is related to the heat of adsorption. The isotherm constants could be determined from a straight line of the q_e versus lnC_e, and the value of K_t and B might be evaluated from the slope and intercept or the straight line, as shown in Fig. 9 c.

All the various isotherm parameters for Cr(VI) adsorption onto MoS$_2$/GO are summarized in Table 3. As presented in Table 3, the correlation coefficient R^2 of Langmuir isotherm was higher than both that of Freundlich isotherm and that of Temkin isotherm, which confirmed that Langmuir isotherm was the most appropriate model to fit the experimental data for Cr(VI) adsorption on MoS$_2$/GO. It illustrates that Cr(VI) adsorption on MoS$_2$/GO, which took place at specific homogeneous sites, was monolayer bonding process. The maximum adsorption capacity of Cr(VI) adsorption on MoS$_2$/GO was calculated to be 43.95 mg·g^{-1} according to the Langmuir model. And according to Freundlich isotherm model, the values of n were greater than 1 which implied a strong interaction between Cr (VI) and MoS$_2$/GO, and the sorption was a favourable process.

3.8. Adsorption thermodynamics

The activation energy (E_a) is the minimum energy required to overcome for the adsorptive reaction to occur [25]. The higher value of E_a indicated that the driving force need to be overcome between the adsorbent and adsorbate will be greater in the adsorption process. In addition, E_a is also a judgment to determine the adsorption type, whether physic-sorption or chemic-sorption. Weak van der Waals forces are responsible in case of physical adsorption and its activation energy is below 4.18 kJ·mol^{-1} [26]. However, when the value of E_a is more than 4.18 kJ·mol^{-1}, which might be an index of chemical adsorption or reduction reactions. The Arrhenius equation gives the quantitative basis of the relationship between the activation energy and the rate at which a reaction proceeds, which is expressed by Eq. 10:

$$\ln k_2 = \ln A - \frac{E_a}{RT},\qquad(10)$$

where, E_a (kJ·mol^{-1}) is the activation energy, k_2 is the pseudo-second kinetic rate constants at different temperatures, A is Arrhenius factor, R (8.314 J·mol^{-1}·K^{-1}) is the gas constant and T(K) is the absolute temperature. E_a could be obtained from the slope of the linear plots of lnk_2 versus $1/T$, as shown in Fig. 10.
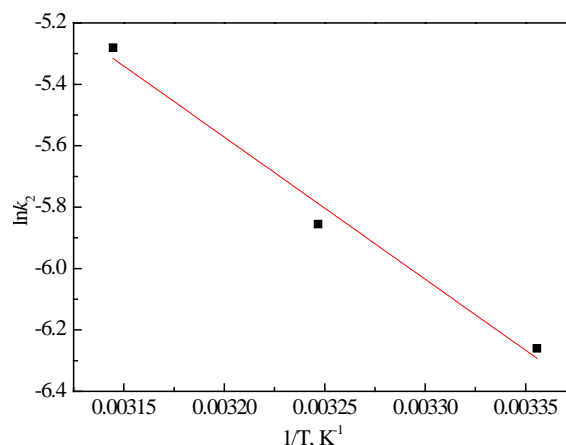
Fig. 10. Plot of lnk$_2$ versus 1/T for Cr(VI) adsorption on MoS$_2$/GO

The calculated value of E_a for the adsorption of Cr(VI) on MoS$_2$/GO was to be approximately 38.5 kJ·mol^{-1}, which was more than 4.18 kJ·mol^{-1}, indicating that the process might be an activated chemical adsorption.

It is meaningful to comprehend the adsorption mechanism and determine whether the process of Cr(VI) adsorption on MoS$_2$/GO is spontaneous or not via thermodynamic analysis.

Table 3. The constants of adsorption isotherms

Langmuir			Freundlich			Temkin		
q_{max}, mg·g^{-1}	K_L, L·mg^{-1})	R^2	K_F, mg·g^{-1}(L·mg^{-1})$^{1/n}$	n	R^2	K_T, L·g^{-1}	B	R^2
43.95	4.96	0.9996	29.78	8.46	0.5117	12600	3.38	0.6184

To further investigate the adsorption thermodynamics of Cr(VI) uptake on MoS$_2$/GO surface, the adsorption experiments were carried out at various temperatures (298, 308 and 318 K). The thermodynamic parameters such as Gibbs free energy, enthalpy and entropy of the adsorption process can be obtained from the follow equations:

$$\ln K = \frac{-\Delta H}{RT} + \frac{\Delta S}{R} ; \qquad (11)$$

$$\Delta G = \Delta H - T\Delta S , \qquad (12)$$

where ΔG (kJ·mol^{-1}), ΔH (kJ·mol^{-1}) and ΔS (J·mol^{-1}·K^{-1}) represent Gibbs free energy, enthalpy and entropy, respectively. K (q_e/C_e) is an equilibrium constant at various temperatures and R is the gas constant (8.314 J·mol^{-1}·K^{-1}), T denotes the temperature. The values of ΔH and ΔS could be calculated from the slope and intercept of the linear plot of $\ln K$ versus $1/T$, which was shown in Fig. 11.
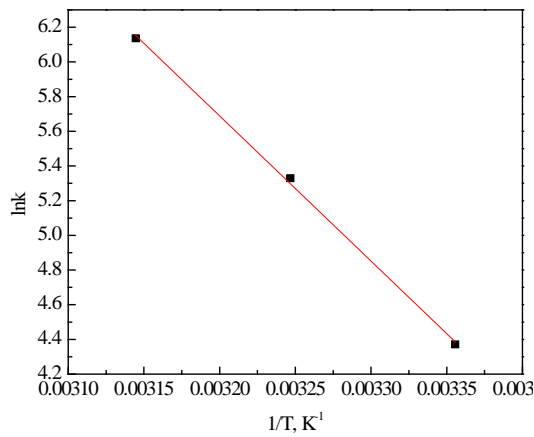
Fig. 11. Plot of ln$K$ versus 1/T for Cr(VI) on MoS$_2$/GO

The thermodynamic parameters for Cr(VI) adsorption on MoS$_2$/GO are listed in Table 4. The positive value of ΔH confirmed that adsorption was an endothermic process. The positive value of ΔS indicated the increased randomness at the solid/liquid interface during the Cr(VI) sorption, which reflected the fact that Cr(VI) had a good affinity for MoS$_2$/GO [27]. The values of ΔG at various temperatures were found to be negative, which suggested the feasibility and spontaneity of the sorption process. The calculated values of ΔG for Cr(VI) adsorption on MoS$_2$/GO were -10.86 kJ·mol^{-1}, -13.56 kJ·mol^{-1} and -16.26 kJ·mol^{-1} at 298 K, 308 K and 318 K, respectively. The decrease in ΔG values with the rising temperature indicated that temperature increasing was favourable for the adsorption process.

The adsorption was regarded as physical process if $\Delta H < 40$ kJ·mol^{-1}, in which there was van der Waals interaction between the adsorbent and adsorbate. And if $\Delta H > 40$ kJ·mol^{-1}, the adsorption was regarded as chemical adsorption, in which there was chemical bonding between the adsorbent and adsorbate [28]. The calculated value of enthalpy (ΔH) for the adsorption of Cr(VI) on MoS$_2$/GO was 69.57 kJ·mol^{-1}, which further confirmed the adsorption process might be mainly belong to chemical adsorption, corresponding to the conclusion from E_a result. In summary, the adsorption thermodynamics investigation proved that the Cr(VI) adsorption on the surface of MoS$_2$/GO was a spontaneous endothermic chemical process.

3.9. Influence of organic contamination coexisting

Organic pollutants exist inevitably in the environmental water practically, and humus is the widespread form of organic contamination. Therefore, humic acid (HA) was chosen as the typical organic pollutant to explore the influence of organics coexistence on the adsorption removal of Cr(VI). HA has a large specific surface area and complex structure with a variety of active functional groups, such as hydroxyl, carboxyl, carbonyl, methoxy and so on. Hence it displayed high reactivity and strong complexation with metal ions. Since the content of HA in water was small, and the influence of HA with various concentrations from 10 mg·L^{-1} to 50 mg·L^{-1} on the removal of Cr (VI) was investigated in this experiment. The adsorption efficiency of MoS$_2$/GO for Cr(VI) removal with HA coexisting was presented in Fig. 12. Obviously, it took ca.300 min to reach adsorption equilibrium without HA coexisting, at which about 99.7 % of Cr(VI) was removed. While it took only no more than 40 min to reach adsorption equilibrium, at which the removal efficiency of Cr(VI) 98.8 %, 99.4 % and 99.7 % were removed when the concentration of HA were 10 mg·L^{-1}, 30 mg·L^{-1} and 50 mg·L^{-1} respectively. There was almost no difference in the influence of various concentration of HA on the removal efficiency of Cr(VI). It indicated that the adsorption efficiency of MoS$_2$/GO was improved significantly after the addition of HA and the time to reach equilibrium was shortened greatly. The experimental results elucidated that coexistence of organic contaminant would enhance the adsorption removal of Cr(VI) practically.
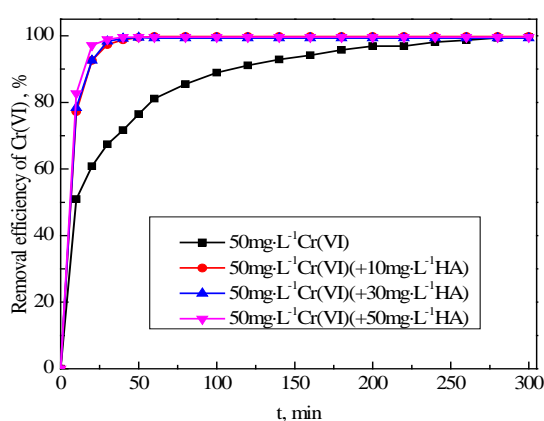
Table 4. Thermodynamic parameters for Cr(VI) adsorption

T, K	$q_{e,cal}$, mg·g^{-1}	k_2, 10^{-2} min^{-1}	E_a, kJ·mol^{-1}	R^2	ΔG, kJ·mol^{-1}	ΔH, kJ·mol^{-1}	ΔS, J·mol^{-1}·K^{-1}
298	19.45	0.191	38.5	0.9927	-10.86	69.57	269.9
308	21.71	0.286	–	0.9807	-13.56	–	–
318	22.63	0.508	–	0.9904	-16.26	–	–

Fig. 12. Effect of HA of adsorption of Cr(VI) on MoS₂/GO

3.10. Desorption and reusability

The essential requirement of an adsorbent was its potential to be recovered and reused. After the completion of adsorptive experiments, the adsorbent was collected. The adsorbent was desorbed at 25°C with 100 mL of different concentrations of NaOH solution ($0.1 \ mol \cdot L^{-1}$, the desorption time was 2 h), and the MoS₂/GO was reused after regeneration. Several adsorption-desorption cycles were made and the adsorption capacities of adsorbents for Cr(VI) were examined, which was illustrated in Fig. 13. It showed the adsorption capacity decreased from 43.95, 43.47, 41.84, 40.88, 40.42 $mg \cdot g^{-1}$ with the utilization frequency increased. The decline of adsorption capacities was about 8.0 % for MoS₂/GO after reused for five times, which elucidated that the adsorbent could be recycled in the removal of Cr(VI).
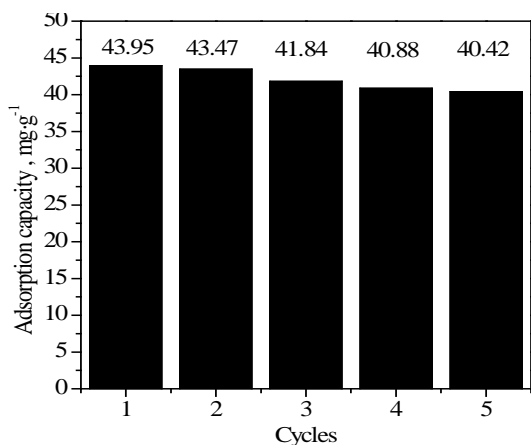

Fig. 13. Recycling of MoS₂/GO for the adsorption of Cr(VI)

4. CONCLUSIONS

The rod-like nano-MoS₂/GO was fabricated via a simple hydrothermal, which was proved to be a promising absorbent to remove Cr(VI) from aqueous solution. The investigation on adsorption kinetics and isotherms showed that pseudo-second-order kinetics and Langmuir isotherm model fit well the experimental data. The adsorption rate was mainly controlled by both exterior and interior surface diffusion steps. The adsorption thermodynamics proved that the Cr(VI) adsorption on MoS₂/GO was an endothermic and spontaneous chemi-sorption process. The maximum

adsorption capacity was 43.95 $mg \cdot g^{-1}$ and the adsorption efficiency of Cr(VI) was enhanced significantly with organic contamination coexisting. After recycling five times, the decline of adsorption capacity of MoS₂/GO was about 8.0%, which indicated that the adsorbents could be recycled in the removal of Cr(VI). The MoS₂/GO nanocomposite has been proved to be a low-cost, efficient and promising adsorbent used for heavy metal ions removal from wastewater.

REFERENCES

1. **He, Y., Li, B.B., Zhang, K.N., Li, Z., Ye, W.M.** Experimental and Numerical Study on Heavy Metal Contaminant Migration and Retention Behavior of Engineered Barrier in Tailings Pond *Environmental Pollution* 252 2019: pp. 1010 – 1018. https://doi.org/10.1016/j.envpol.2019.06.072

2. **Tarek, E.K., Amel, F.E., Ali, E., Nagwa, M.I.** Functionalized Chitosan Nanocomposites for Removal of Toxic Cr (VI) from Aqueous Solution *Reactive and Functional Polymers* 146 2020: pp. 104407 – 104421. https://doi.org/10.1016/j.reactfunctpolym.2019.104407

3. **Yang, H.F., Shen, K., Fu, P., Zhang, G.** Preparation of a Novel Carbonaceous Material for Cr(VI) Removal in Aqueous Solution Using Oily Sludge of Tank Bottom as a Raw Material *Journal of Environmental Chemical Engineering* 7 2019: pp. 102898 – 102905. https://doi.org/10.1016/j.jece.2019.102898

4. **Chatterjee, S., Mahanty, S., Das, P., Chaudhuri, P., Das, S.** Biofabrication of Iron Oxide Nanoparticles Using Manglicolous Fungus Spergillus Niger BSC-1 and Removal of Cr(VI) from Aqueous Solution *Chemical Engineering Journal* 385 2020: pp. 123790 – 123802. https://doi.org/10.1016/j.cej.2019.123790

5. **Vikraman, D., Karuppasamy, K., Hussain, S., Kathalingam, A., Sanmugam, A., Jung, J., Kim, H. S.** One-pot Facile Methodology to Synthesize MoS2-graphene Hybrid Nanocomposites for Supercapacitors with Improved Electrochemical Capacitance *Composites Part B* 161 2019: pp. 555 – 563. https://doi.org/10.1016/j.compositesb.2018.12.143

6. **Meng, X.Y., Yu, L., Ma, C., Nan, B., Si, R., Tu, Y.C., Deng, J., Deng, D.H., Bao, X.H.** Three-dimensionally Hierarchical MoS₂/graphene Architecture for High-performance Hydrogen Evolution Reaction *Nano Energy* 61 2019: pp. 611 – 616. https://doi.org/10.1016/j.nanoen.2019.04.049

7. **Theerthagiri, J., Senthil, R.A., Senthilkumar, B., Polu, A.R., Madhavan, J., Ashokkumar, M.** Recent Advances in MoS2 Nanostructured Materials for Energy and Environmental Applications – A Review *Journal of Solid State Chemistry* 252 2017: pp. 43 – 71. https://doi.org/10.1016/j.jssc.2017.04.041

8. **Zhang, L., He, X., Zhou, Q.X., Hu, X.G.** Fabrication of 1T-MoS2 Nanosheets and the High-efficiency Removal of Toxic

Metals in Aquatic Systems: Performance and Mechanisms *Chemical Engineering Journal* 386 2020: pp. 123996. https://doi.org/10.1016/j.cej.2019.123996

9. **Tian, H., He, J.H., Hu, M.H.** A Selectivity-controlled Adsorbent of Molybdenum Disulfide Nanosheets Armed with Superparamagnetism for Rapid Capture of Mercury Ions *Journal of Colloid and Interface Science* 551 2019: pp. 251 – 260. https://doi.org/10.1016/j.jcis.2019.05.027

10. **Nguyen, T.K., Jeong, S., Manavalan, K., Youn, J.S., Park, C.M., Jeon, K.J.** Controllable Desulfurization in Single Layer MoS_2 by Cationic Current Treatment in Hydrogen Evolution Reaction *Applied Surface Science* 507 2020: pp. 145181. https://doi.org/10.1016/j.apsusc.2019.145181

11. **Gao, Y., Chen, C.L., Tan, X.L., Xu, H., Zhu, K.R.** Polyaniline-modified 3D-flower-like Molybdenum Disulfide Composite for Efficient Adsorption/photocatalytic Reduction of Cr(VI) *Journal of Colloid and Interface Science* 476 2016: pp. 62 – 70. https://doi.org/10.1016/j.jcis.2016.05.022

12. **Bai, X., Du, Y.Y., Hu, X.Y., He, Y.D., He, C.L., Liu, E.Z., Fan, J.** Synergy Removal of Cr (VI) and Organic Pollutants Over $RP-MoS_2/rGO$ Photocatalyst *Applied Catalysis B: Environmental* 239 2018: pp. 204 – 213. https://doi.org/10.1016/j.apcatb.2018.08.016

13. **Li, Z.H., Wang, L., Li, Y., Feng, Y.Y., Feng, W.** Carbon-based Functional Nanomaterials: Preparation, Properties and Applications *Composites Science and Technology* 179 2019: pp. 10 – 40. https://doi.org/10.1016/j.compscitech.2019.04.028

14. **Liu, X.L., Ma, R., Wang, X.X., Ma, Y., Yang, Y.P., Zhuang, L., Zhang, S., Jehan, R., Chen, J.R., Wang, X.K.** Graphene Oxide-based Materials for Efficient Removal of Heavy Metal Ions from Aqueous Solution: A Review *Environmental Pollution* 252 2019: pp. 62 – 73. https://doi.org/10.1016/j.envpol.2019.05.050

15. **Jeon, C.** Removal of Cr(VI) from Aqueous Solution Using Amine-impregnated Crab Shells in the Batch Process *Journal of Industrial and Engineering Chemistry* 77 2019: pp. 111 – 117. https://doi.org/10.1016/j.jiec.2019.04.025

16. **Harrison, D.R., Gregory, T., Jonathan, L.S.** Reduced Texaphyrin: A Ratiometric Optical Sensor for Heavy Metals in Aqueous Solution *Frontiers of Chemical Science and Engineering* 14 (1) 2020: pp. 19 – 27. https://doi.org/10.1007/s11705-019-1888-y

17. **Wan, S.L., He, F., Wu, J.Y., Wan, W.B., Gu, Y.W., Gao, B.** Rapid and Highly Selective Removal of Lead from Water Using Graphene Oxide-hydrated Manganese Oxide Nanocomposites *Journal of Hazardous Materials* 314 2016: pp. 32 – 40. https://doi.org/10.1016/j.jhazmat.2016.04.014

18. **Yuan, R., Yuan, J., Wu, Y.P., Ju, P.F., Ji, L., Li, H.X., Chen, L., Zhou, H.D., Chen, J.M.** Graphene Oxide-Monohydrated Manganese Phosphate Composites: Preparation via Modified Hummers Method *Colloids and Surfaces A: Physicochemical and Engineering Aspects* 547 2018: pp. 56 – 63.

19. **Tavker, N., Sharma, M.** Designing of Waste Fruit Peels Extracted Cellulose Supported Molybdenum Sulfide Nanostructures for Photocatalytic Degradation of RhB Dye and Industrial Effluent *Journal of Environmental Management* 255 2020: pp. 109906. https://doi.org/10.1016/j.jenvman.2019.109906

20. **Yan, L.G., Li, S., Yu, H.Q., Shan, R.R., Du, B., Liu, T. T.** Facile Solvothermal Synthesis of Fe_3O_4/bentonite for Efficient Removal of Heavy Metals from Aqueous Solution *Powder Technology* 301 2016: pp. 632 – 640. https://doi.org/10.1016/j.powtec.2016.06.051

21. **Yang, L.J., Zhang, Y.Y., Liu, X.Y., Jiang, X.Q., Zhang, Z.Z., Zhang, T.T., Zhang, L.** The Investigation of Synergistic and Competitive Interaction between Dye Congo Red and Methyl Blue on Magnetic $MnFe_2O_4$ *Chemical Engineering Journal* 246 2014: pp. 88 – 96. https://doi.org/10.1016/j.cej.2014.02.044

22. **Tang, L., Zhang, S., Zeng, G.M., Zhang, Y., Yang, G.D., Chen, J., Wang, J.J., Wang, J.J., Zhou, Y.Y., Deng, Y.C.** Rapid Adsorption of 2,4-dichlorophenoxyacetic Acid by Iron Oxide Nanoparticles-doped Carboxylic Ordered Mesoporous Carbon *Journal of Colloid and Interface Science* 445 2015: pp. 1 – 8. https://doi.org/10.1016/j.jcis.2014.12.074

23. **Matouq, M., Jildeh, N., Qtaishat, M., Hindiyeh, M., Syouf, M.Q.A.** The Adsorption Kinetics and Modeling for Heavy Metals Removal from Wastewater by Moringa Pods *Journal of Environmental Chemical Engineering* 3 (2) 2015: pp. 775 – 784. https://doi.org/10.1016/j.jece.2015.03.027

24. **Jeppu, G.P., Clement, T.P.** A Modified Langmuir-Freundlich Isotherm Model for Simulating pH-dependent Adsorption Effects *Journal of Contaminant Hydrology* 129 – 130 2012: pp. 46 – 53. https://doi.org/10.1016/j.jconhyd.2011.12.001

25. **Sirisomboon, P., Posom, J.** On-line Measurement of Activation Energy of Ground Bamboo Using Near Infrared Spectroscopy *Renewable Energy* 133 2019: pp. 480 – 488. https://doi.org/10.1016/j.renene.2018.10.051

26. **Duranoglu, D., Trochimczuk, A.W., Beker, U.** Kinetics and Thermodynamics of Hexavalent Chromium Adsorption onto Activated Carbon Derived from Acrylonitrile-divinylbenzene Copolymer *Chemical Engineering Journal* 187 2012: pp. 193 – 202. https://doi.org/10.1016/j.cej.2012.01.120

27. **Liang, F., Song, Y., Huang, C., Zhang, J., Chen, B.** Adsorption of Hexavalent Chromium on a Lignin-based Resin: Equilibrium, Thermodynamics, and Kinetics *Journal of Environmental Chemical Engineering* 1 (4) 2013: pp. 1301 – 1308. https://doi.org/10.1016/j.jece.2013.09.025

28. **Yang, J.B., Yu, M.Q., Qiu, T.** Adsorption Thermodynamics and Kinetics of Cr(VI) on KIP210 Resin *Journal of Industrial and Engineering Chemistry* 20 (2) 2014: pp. 480 – 486. https://doi.org/10.1016/j.jiec.2013.05.005